

# NUMERICAL SIMULATION OF FATIGUE CRACK GROWTH IN THE ADHESIVE BONDLINE OF HYBRID CFRP JOINTS

R. Sachse\*, A.K. Pickett\*, M. Käß\*, P. Middendorf\*

\*Institute of Aircraft Design, University of Stuttgart  
Pfaffenwaldring 31, 70569 Stuttgart  
[sachse@ifb.uni-stuttgart.de](mailto:sachse@ifb.uni-stuttgart.de)

**Key words:** fatigue simulation, hybrid composite joints, crack propagation

**Summary:** *This paper presents the implementation and application of a constitutive model for simulation of crack propagation in adhesively bonded CFRP joints subjected to high cycle fatigue loading. The model extends a static cohesive zone model using an additional fatigue damage variable that is computed based on the Paris law curve. Results show the model is able to closely predict the influence of a mechanical fastener on the crack growth behavior in adhesive bondline. Two important features of the model are fatigue degradation, which is limited to integration points located at the crack tip, and the application of several non-local algorithms to predict crack advance.*

## 1 INTRODUCTION

Due to an increased application of carbon fiber reinforced plastics (CFRP) in the aerospace and automotive industry, joining of the structures becomes a central issue in the design process. While commonly used mechanical fasteners show significant disadvantages in combination with CFRP, adhesive bonding can be considered a promising alternative as the load transfer between the two sheets is distributed and undesirable cutting of continuous fibers is avoided. However, undetectable weakbonds can result in local stress concentrations and premature failure. Particularly under high cyclic fatigue loading several researches have shown that cracks in the adhesive bondline can propagate at loads well below the adhesive static strength. Consequently, according to AC20-107B [2] aerospace structural joints must use a hybrid combination of mechanical and adhesive bonding. [1] [3] [4] [5] [6]

The EU funded FP7 project BOPACS [1] aims to investigate the application of features that can arrest a crack in the adhesive bondline and prevent catastrophic failure of the joint. Recent studies by the authors have indicated that the rivetless nut plate joint [7] is able to effectively slow crack growth in the adhesive bondline under realistic aircraft loading conditions. The effect on the crack growth, however, varies significantly depending on the distances to the rivetless nut plate joint and can lead to curved crack fronts. [8]

An effective application of rivetless nut plate joint in the design process requires a robust simulation of crack propagation under fatigue loading, which must be able to account for arbitrary crack fronts. One method widely used to model quasi-static as well as cyclic delamination in composites and adhesively bonded joints applies cohesive zone models. Different researchers have proposed constitutive models for high-cycle fatigue that describe the evolution of a damage variable by linking damage mechanics and fracture mechanics. The models extract the strain energy release rate amplitude ( $\Delta G$ ) from the cohesive zone element

and use the Paris law curve to determine the rate of crack growth. Therefore, all elements in the cohesive zone ahead of the crack tip are being degraded. In order to satisfy the global Paris-Law, the local damage rate of each Integration Point (IP) requires the computation of a cohesive zone length ahead of the crack tip. This in turn depends on the geometry and loading conditions and prevents the application of these models to complex three-dimensional structures. [9] [10] [11] [12]

Kawashita et al. [12] recently proposed a modification of this approach that eliminates the dependency on the cohesive zone length by degrading only those IP's that belong to the crack tip. Three non-local approaches were used to track the crack front; namely, to determine the direction of propagation, to calculate the effective element length and to extract the strain energy release rate.

This paper presents the implementation of a fatigue damage formulation that partially adapts the method of Kawashita et al. [12]. An alternative approach to calculate the effective element length and crack front direction that can be used for irregular meshes, is proposed. Furthermore, an additional non-local algorithm that adaptively determines the numerical fatigue frequency used for the explicit finite element analysis is presented. The implemented model is then used to predict the influence of a rivetless nut plate joint on the crack propagation in a hybrid mechanical-adhesive bonded CFRP-joint subjected to fatigue loading.

## 2 DESCRIPTION OF STATIC AND FATIGUE DAMAGE MODEL

A constitutive model for an 8-node three-dimensional cohesive zone element (CZE) has been implemented in the commercial software ABAQUS using a user-defined material subroutine for explicit time-integration (VUMAT). It employs the standard cohesive zone approach for quasi-static loading and extends the constitutive model to account for damage related to fatigue loading.

### 2.1 Constitutive model for quasi-static loading

The Cohesive Zone Model (CZM) has been widely used to simulate interfacial fracture for quasi-static loading. It represents the formation of micro-cracks that are assumed to develop in a damage zone behind the crack tip on a macroscopic scale. The evolution of the micro-cracks is comprised within a static damage variable and results in the loss of cohesive stiffness.

The CZM relates traction  $t$  to the relative displacement  $\delta$  of two faces, where only the three displacement components  $\delta_{33}$  for opening mode I, and  $\delta_{13}$  and  $\delta_{23}$  for shear modes II and III are considered. For further evaluations, only mode I normal and resultant mode II shear opponents, as well as the mixed-mode displacement, shall be considered in the following:

$$\delta_I = \langle \delta_{33} \rangle \quad (1)$$

$$\delta_{II} = \sqrt{\delta_{13}^2 + \delta_{23}^2} \quad (2)$$

$$\delta_m = \sqrt{\delta_I^2 + \delta_{II}^2} \quad (3)$$

where  $\langle \cdot \rangle$  is the Macauley bracket, i.e.  $\langle \cdot \rangle = \max(\cdot, 0)$ . The traction components can therefore be calculated using stiffness  $K_I$  and  $K_{II}$  for Mode I and Mode II loading respectively:

$$t_I = \begin{cases} (1 - d_{static})K_I \delta_I, & \delta_I \geq 0 \\ K_I \delta_I, & \delta_I \leq 0 \end{cases} \quad (4)$$

$$t_{II} = (1 - d_{static})K_{II} \delta_{II} \quad (5)$$

A bilinear traction separation law, as shown in Figure 1 (left) is adopted in this paper. It consists of an initial linear elastic region, followed by linear softening representing inelastic damage accumulation. For mixed mode loading the damage initiation starts when the following equation is fulfilled:

$$\left(\frac{\langle t_I \rangle}{t_I^0}\right)^2 + \left(\frac{t_{II}}{t_{II}^0}\right)^2 = 1 \quad (6)$$

In Equation (6),  $t^0$  represents the maximum interfacial traction for pure mode loading. The area below the traction separation curve is equivalent to the critical strain energy release rate  $G_c$  and can be calculated through integration of mixed mode cohesive traction  $t_m$  as a function of mixed-mode displacement  $\delta_m$ :

$$G_c = \int_0^{\delta_m^f} t_m d\delta_m \quad (7)$$

During the numerical simulation a midpoint rule is used at each time step  $t$  to update the instantaneous strain energy release rate  $G^{inst}$ .

$$G_t^{inst} = G_{t-1}^{inst} + \frac{(t_t + t_{t-1})}{2} (\delta_t - \delta_{t-1}) \quad (8)$$

In Equation (7),  $\delta_m^f$  represents the mixed-mode displacement at failure. Under mixed mode loading,  $\delta_m^f$  is calculated to fulfill the power law failure criterion:

$$\left(\frac{G_I}{G_{IC}}\right)^\alpha + \left(\frac{G_{II}}{G_{IIC}}\right)^\alpha = 1 \quad (9)$$

The critical strain energy release rate must be separately specified for pure mode loading. The power coefficient  $\alpha$  is also a material parameter that must ideally be determined through tests. Finally, the static damage variable can be defined in terms of mixed-mode displacement:

$$D_{static} = \frac{\delta_m^f (\delta_m^{max} - \delta_m^0)}{\delta_m^{max} (\delta_m^f - \delta_m^0)} \quad (10)$$

where  $\delta_m^0$  represents the mixed-mode displacement at damage initiation and  $\delta_m^{max}$  the maximum mixed-mode displacement during loading history.

The required displacement components are available in the VUMAT and are provided by the cohesive zone element implemented in ABAQUS. The 8-node three-dimensional cohesive zone element presented in Figure 1 (right) consists of 4 IPs located on the mid-surface of the element.

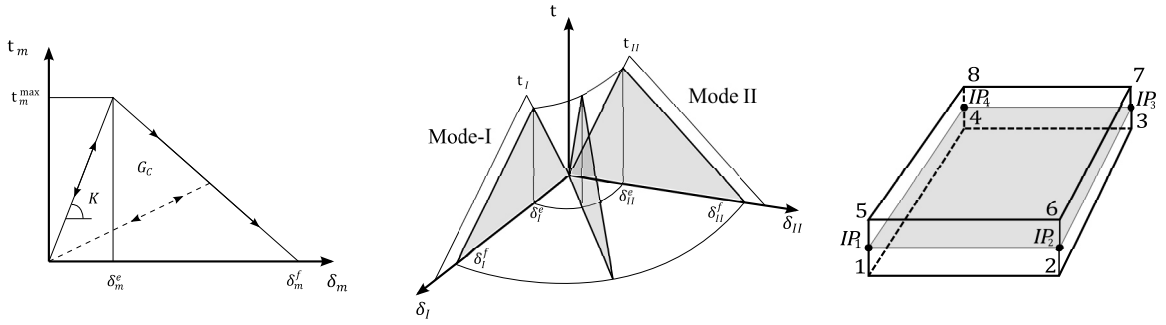


Figure 1: Mixed mode cohesive law (left) and composition from mode I and mode II loading (middle) for static loading; Mixed mode cohesive law including fatigue damage degradation (right)

## 2.2 Constitutive model for high-cycle fatigue loading

High cycle fatigue simulation faces the difficulty of simulating a very large number of repeated loading and unloading that could barely be achieved within a reasonable time frame for real structures. Therefore, an alternative method has been proposed by several authors that can be applied to constant amplitude loading. [9] [10] [11] [12]

In a first step, the maximum fatigue load is introduced quasi-statically. Once dynamic vibrations have been dampened out, the fatigue damage model is activated. Figure 2 compares the actual load curve to the representative load curved used for the simulation. The total damage accumulation  $\dot{D}_{total}$  resulting from a general loading can then be described by the summation of quasi-static  $\dot{D}_{static}$  and fatigue  $\dot{D}_{fatigue}$  damage contributions. [9]

$$\frac{dD_{total}}{dt} = \dot{D}_{total} = \dot{D}_{static} + \dot{D}_{fatigue} \quad (11)$$

In the initial quasi-static loading static damage is accumulated. As described in Section 2.1, this damage is linked to the relative displacement of the interfaces surfaces.

Fatigue damage accumulation can then be described by linking fracture mechanics to damage mechanics. The instantaneous value of the strain energy release rate corresponding to the maximum applied fatigue load  $G_{max}^{inst}$  is used to calculate the strain energy release rate amplitude  $\Delta G$  using the R-ratio from the fatigue test:

$$\Delta G = G_{max}^{inst} - G_{min}^{inst} = (1 - R^2)G_{max}^{inst} \quad (12)$$

In a next step, the crack growth rate  $da/dN$  can be determined from the Paris law curve.

$$\frac{da}{dN} = C_1 \Delta G^{C_2} \quad (13)$$

where  $a$  corresponds to the crack length and  $N$  describes the number of loading cycles. The parameters  $C_1$  and  $C_2$  can be considered as material parameters and are determined from experimental tests.

As shown in Figure 2 the relationship between  $\Delta G$  and the crack growth rate plotted in a double logarithmic diagram, can be divided into three regions. In region I,  $\Delta G$  is smaller than the fatigue threshold  $G_{th}$  and no crack growth can be observed. In region III  $\Delta G$  becomes close to  $G_c$  leading to rapid increase in crack growth close to the quasi-static value.

In region II, however, a linear correlation can be found between  $\Delta G$  and the crack growth rate. This region is described by the Paris law presented in Equation (13) and the model described in this paper shall be limited to this region.

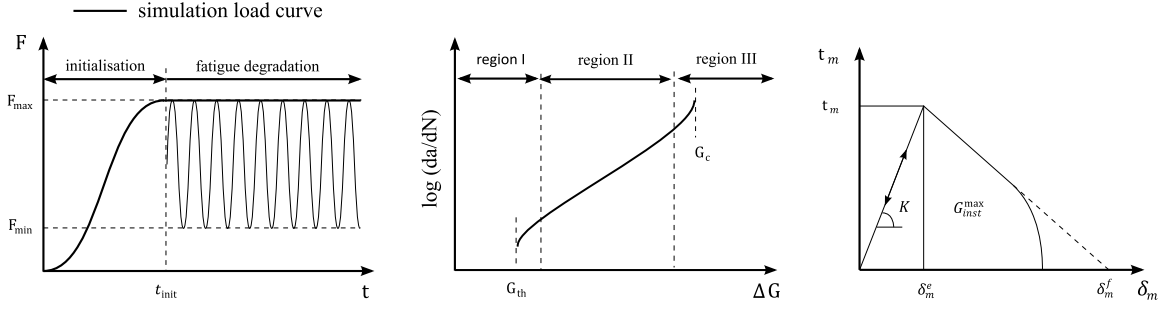


Figure 2: Comparison of numerical and experimental load curve (left); Paris law curve (center); modified traction separation law including fatigue damage (right)

Similar to the critical strain energy release rate  $G_c$ , the Paris law strongly depends on the loading mode. In the absence of more detailed experimental results, a simple linear rule of mixture between mode I and II loading is used:

$$C_1 = \frac{G_I^{inst}}{G_I^{inst} + G_{II}^{inst}} C_{1I} + \frac{G_{II}^{inst}}{G_I^{inst} + G_{II}^{inst}} C_{1II} \quad (14)$$

$$C_2 = \frac{G_I^{inst}}{G_I^{inst} + G_{II}^{inst}} C_{2I} + \frac{G_{II}^{inst}}{G_I^{inst} + G_{II}^{inst}} C_{2II} \quad (15)$$

Based on the mixed-mode crack growth rate  $da/dN$ , the equivalent fatigue damage accumulation  $dD_{fatigue}/dt$  is calculated. Therefore, a link between the number of cycles  $N$  and the timestep of the explicit simulation  $\Delta t$  must be established. Furthermore, the change of crack length  $da$  within the element must be correlated to the change of the scalar fatigue damage variable  $dD_{fatigue}$ .

Given an effective length of a cohesive element  $l_e$ , which must be cracked for complete decohesion due to fatigue loading, the corresponding number of fatigue cycles  $\Delta N_e$  can be calculated based on the crack growth rate:

$$\Delta N_e = \frac{dN}{da} l_e \quad (16)$$

The fatigue damage  $D_{fatigue}$  that must be accumulated after quasi-static loading for complete decohesion equals  $1 - D_{static}$ . Therefore the fatigue damage rate with respect to the number of cycles can be expressed as follows:

$$\frac{dD_{fatigue}}{dN} = \frac{\Delta D_{fatigue}}{\Delta N} = \frac{1 - D_{static}}{\Delta N_e} \quad (17)$$

Assuming that for each time step of the explicit simulation, a certain number of loading cycles is represented, the fatigue damage can be expressed by defining a numerical fatigue frequency  $f_{num}$ :

$$D_{fatigue}^t = D_{fatigue}^{t-1} + \frac{dD_{fatigue}}{dN} \cdot f_{num} \cdot \Delta t \quad (18)$$

where the superscripts  $t$  indicates the current time step and  $f_{num}$  is defined as:

$$f_{num} = \frac{dN}{dt} \quad (19)$$

### 2.3 Nonlocal algorithms

Previously developed fatigue models [9] [10] allow the fatigue degradation of every element in the fracture process zone. In order to correctly represent the global Paris law, the local fatigue damage rate must be corrected by the cohesive zone length. Approaches to calculate this length have been limited to analytical solutions for certain specimens, or require additional quasi-static simulations. An application to complex and changing crack fronts is therefore limited. [12]

In order to avoid the computation of a cohesive zone length, fatigue damage shall be limited to IP's belonging only to the crack tip as proposed by Kawashita et.al. [12]. Furthermore, the fatigue model must be applicable to irregular meshes, which is necessary for complex structures containing holes or cut-outs. Finally, the model should be insensitive to variable crack growth rates. This ensures computational efficiency when the crack growth changes due to the effect of crack arresting features. These requirements can be achieved by considering the following non-local aspects during simulation:

- Crack tip monitoring
- Computation of crack growth direction
- Computation of an effective element length
- Computation of an adaptive numerical fatigue frequency

The application of non-local algorithms is achieved by using an external “communication” text file, which allows the transfer of information between IP's. A python script has been developed, which acts as a preprocessor after the simulation model has been set up. It reads the model input file and writes a text file containing all relevant information for the communication subroutine. This includes the following information:

- Coordinates of the IP and element ID associate to it used for identification of the IP within the user-material subroutine
- List of neighbor IPs used for crack tip monitoring and the computation of crack growth direction
- Surface coordinates and center coordinates associated to IP user for computation of crack growth direction
- Instantaneous strain energy release rate for mode I and mode II used for computation of adaptive numerical fatigue frequency
- Markers used to trigger certain communication algorithms

During a simulation the user material subroutine is able to access and to modify the communication text file.

In order to apply the nonlocal algorithms, an assumption was made including a modified location of the IP and a definition of the associated surface area. As presented in Figure 1, ABAQUS defines the location of the IP of the cohesive zone element at the endpoints of the mid-surface. For computation of the non-local algorithms, the mid-surface is split into four squares as shown in Figure 3 (left). Each square is defined by one endpoint and the center of the cohesive surface, as well as the midpoint of two edges attached to the endpoint. The resulting square corresponds to the IP located at the endpoint. The center of the square is assumed to be the location of the IP used for the non-local algorithms.

### 2.3.1 Crack tip monitoring

During the preprocessing phase using the python script, a fatigue degradation marker is set to 1 for user defined IPs, identifying them as part of the initial crack tip. When an IP has failed the fatigue degradation marker is set to 2. Furthermore, the IP informs its neighbor IPs that they now belong to the crack tip. This is done by setting the fatigue marker of the appropriate neighbor IP to 1 within the communication text file. A *von Neumann* neighborhood definition has been defined for the crack tip communication, including all neighbor IPs with which the IP square shares a common edge. In Figure 3 (center), the IP squares numbered 2, 3 and 4 belonged to the initial crack tip. Square 1 has already failed. Square 2 failed in the current time step and informs squares 1, 3 and 5 this has occurred. While square 1 is already failed and square 3 is already in the crack tip, square 5 becomes a new member.

### 2.3.2 Computation of the crack growth direction

The crack growth direction associated to an IP is defined based on the state of fatigue degradation of neighbor IPs. Here, a *Moore* neighborhood definition is used, including all neighbor IP's with which the IP square shares a common endpoint. When an IP fails it informs all IP's in its *Moore* neighborhood and writes down its unique ID. This is the indication for the neighbor IP's to perform a new computation of the crack growth direction, which is then used to calculate the effective element length.

The computation of crack growth direction is presented in Figure 3 (center). Starting from the neighbor IP (square 2), that has informed the current IP (square 5) about its failure, a search is made for the next neighbor IP in the clock-wise direction that is currently in a state of fatigue damage, i.e. the fatigue marker equals 1 (square 4). The ID of the neighbor IP is stored and the same search is performed counter-clockwise (square 3). A vector is constructed between the centers of the neighbor IPs, representing the crack tip tangent. The normal vector to the tangent vector is then defined as the crack growth direction vector.

Although squares 4 and 3 in Figure 3 (center) are already part of the crack tip, the crack tip has changed within their *Moore* neighborhood and a new crack growth direction must therefore be determined.

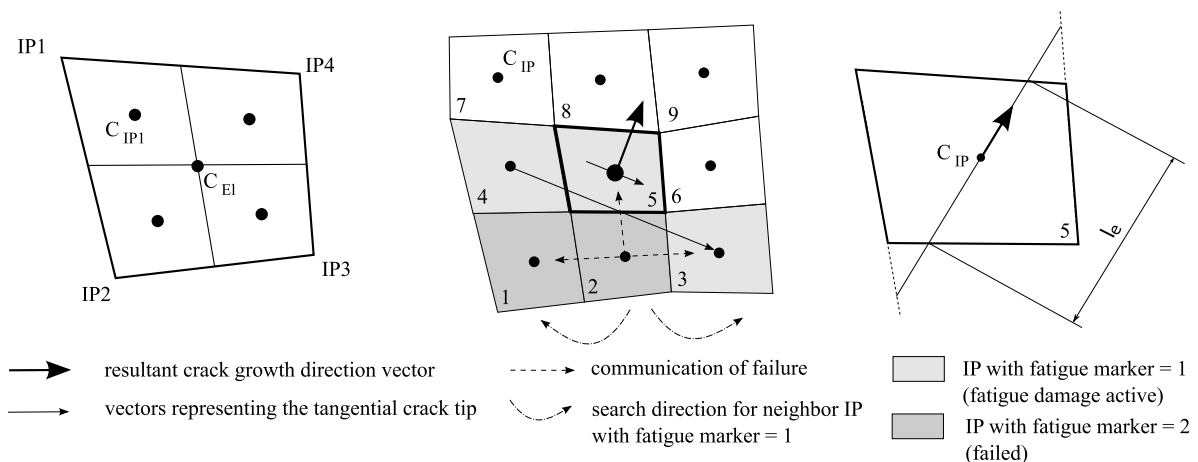


Figure 3: IP square definition (left); crack growth direction computation (center); effective crack length computation (right)

### 2.3.3 Computation of effective element length

The effective element length  $l_e$  must be computed for all IP's within the crack tip. As shown in Figure 3 (right), this length is defined based on the crack growth direction and the geometry of the square associated to the IP. From the IP coordinate corresponding to the center of the square, the intersection of the crack growth direction vector, with vectors along the edges of the square, is computed. The distance between the intersection points closest the center is then defined as the effective element length  $l_e$ .

### 2.3.4 Computation of an adaptive numerical fatigue frequency

The numerical fatigue frequency defines the block of cycles that are represented during a time step. Therefore, it defines the simulation time required for an element to degrade due to fatigue damage as well as the total simulation time required to achieve a certain crack length. During each time step a linear extrapolation is performed. Consequently, the accuracy of the results are influenced by the numerical frequency. Furthermore, the dynamic stability of the simulation, i.e. its tendency to unwanted dynamic vibrations, depends on the damage change during each time step and is therefore also a function of the numerical fatigue frequency.

During a fatigue simulation, the loading on the crack can change, resulting locally in a reduced or increased crack growth rate. Defining a constant numerical frequency throughout the simulation could lead to either dynamic instability, or a very long simulation time to achieve a certain crack growth. It is therefore beneficial to allow the numerical frequency to be adapted based on the current state of loading of crack tip IP's. This is achieved by another non-local algorithm. The numerical fatigue frequency shall be defined based on a user defined number of time-steps  $n_{\Delta t_{fail}}$  required for an IP to be fully degraded due to fatigue damage. The "ideal" numerical fatigue damage can therefore be calculated for an IP using Equation (19):

$$f_{virtual} = \frac{\Delta N_e}{\Delta t_{fail}} = \frac{\Delta N_e}{n_{\Delta t_{fail}} \Delta t} \quad (20)$$

To ensure consistency, only one numerical frequency can be used during a time-step. Considering all IPs within the crack tip, the lowest frequency must be used in order to avoid that IP's with a faster crack growth rate are degraded too quickly.

## 3 TEST SETUP AND MODEL DESCRIPTION

The Cracked Lap Shear specimen (CLS) was used to investigate the effect of a rivetless nut plate joint on crack growth in an adhesively bonded CFRP joint. The CLS specimen provides a section of approximately constant crack growth rate [8] and therefore allows a direct evaluation of the effect of the mechanical fastener. Figure 4 presents a schematic drawing of the test specimen.

The base laminate was made from Hexply IM7/8552 UD prepreg, with a stacking sequence of  $[0^\circ, 45^\circ, 90^\circ, -45^\circ, -45^\circ, 90^\circ, 45^\circ, 0^\circ]_s$ . The 2mm thick plates were bonded using Scotch-Weld 9323 B/A structural adhesive from 3M. The rivetless nut plate joint was installed during the bonding process. The location of the rivetless nut plate joint was selected to be approximately in the middle of the section having a constant crack growth rate. The crack growth was monitored using USB camera microscopes mounted to the edges of the specimen, as well as an automated air-coupled ultrasonic measurement systems to measure crack growth over the specimen width. A detailed description of the specimen, the manufacturing process and the test setup is given by Sachse et. al. [8].

A numerical simulation was performed using the methods outlined in section 2 and the numerical model shown in Figure 4. The laminate was modelled with continuum shell elements assigning a linear elastic anisotropic material model. A quasi-isotropic stacking sequence was assigned identical to the test specimen. The adhesive was represented by 3D cohesive zone elements. The material properties for the laminate and the adhesive are given in Table 1 and Table 2.

The rivetless nut plate joint was modelled using fully integrated solid elements. Figure 5 compares the numerical model to the micro-section of a hybrid adhesively bonded rivetless nut plate joint. Contact interfaces, using a penalty contact method, were defined at the interfaces between the bolt and the laminate, the nut and the retainer, as well as the retainer and the laminate. Tied interfaces were used to connect the bolt with the adhesive and the retainer.

In order to reduce computational time a symmetric half model was used. Figure 4 summarizes the applied boundary conditions. The load was introduced using a pressure load equivalent to the maximum fatigue load. Tabs used in the experiment were not modelled and boundary constraints were applied at the end of the gauge length of the specimen.

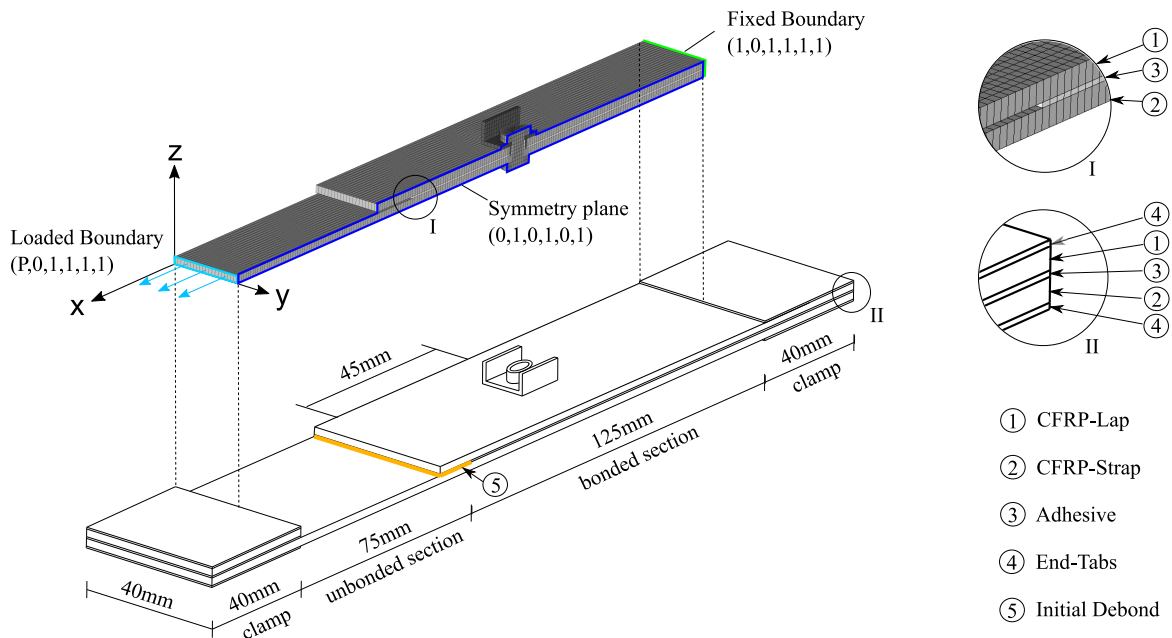


Figure 4: Schematic drawing and numerical model of the adhesively bonded CLS specimen including a rivetless nut plate joint

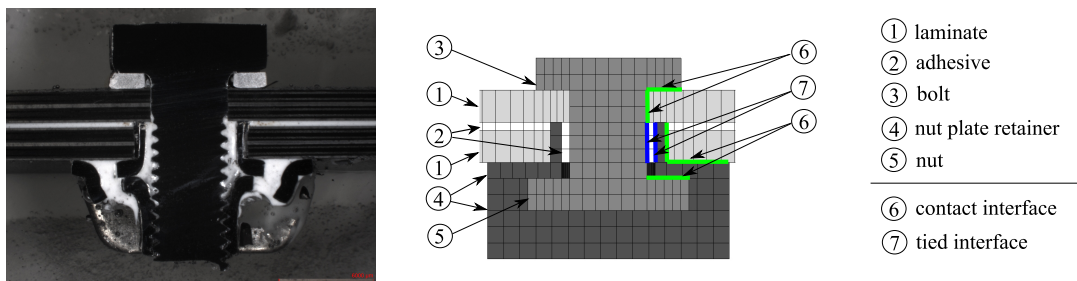


Figure 5: Micro-section (left) and numerical model (right) of rivetless nut plate joint

$E_1$	$E_2, E_3$	$\nu_{12}, \nu_{13}$	$\nu_{23}$	$G_{12}, G_{13}$	$G_{23}$	$t$
[MPa]	[MPa]	–	–	[MPa]	[MPa]	[mm]
163000	96000	0.31	0.45	5400	4900	0.125

Table 1: Material properties of Hexply IM7/8552

$K_I$	$K_{II}$	$t_I^0$	$t_{II}^0$	$G_{Ic}$	$G_{IIc}$	$C_{1CLS}$	$C_{2CLS}$
[N/mm <sup>3</sup> ]	[N/mm <sup>3</sup> ]	[MPa]	[MPa]	[N/mm]	[N/mm]	[mm/cyc]	–
2800	1000	15	10	500	7000	0.00674	2.47

Table 2: Material properties of Scotch-Weld 9323 B/A

#### 4 SIMULATION RESULTS AND DISCUSSION

In a first step, a CLS specimen, without a rivetless nut plate installed, was simulated to verify capability of the constitutive model to correctly predict the crack growth under high cycle fatigue loading. A parameter study was performed to investigate the influence of the mesh size, as well as the number of time-steps  $n_{\Delta t_{fail}}$  used for the calculation of the fatigue frequency. Based on this pre-study a set of parameters was selected for this study and used to numerically predict the Paris law curve. Previously, the Paris law curve parameters were determined through experimental tests and used as an input for the simulation (Table 2). The crack growth rate was numerically computed for four load levels, applying the same approach as used to evaluate the experimental test results. As shown in Figure 6, the numerical model was able to closely predict the Paris law curve for the CLS-specimen, without the need for an additional simulation, or specific analytical equations, to calculate the cohesive zone length.

For a pure adhesive bonded CLS-specimen the crack grows as a uniform straight line, whereas for a hybrid adhesive-rivetless nut plate joint the crack growth is non-uniform. Figure 7 presents the crack length plotted against number of fatigue cycles, where crack growth was measured on the edge of the specimen during testing. After an initial constant crack growth, the crack is slowed significantly after passing the rivetless nut plate joint.

Figure 8 shows the fracture surface of the hybrid CLS-specimen after 1,000,000 cycles, where the specimen was manually detached after the fatigue test. The remaining white adhesive on the surface indicates the crack front at the end of the fatigue test. The hole represents the location of the mechanical fastener. The fracture surface clearly shows the influence of the rivetless nut plate joint on the crack growth which was also found to vary over the specimen width, so that the crack front becomes significantly curved.

The arbitrary crack front resulting from the rivetless nut plate joint poses an additional challenge for the numerical fatigue model. In a first attempt, a fatigue simulation of the hybrid joints was performed without accounting for the influence of the mixed mode ratio. Figure 7 shows that this model does predict an influence of the rivetless nut plate joint, but results do not agree well to test measurements. Consequently, the influence of the mixed mode ratio was studied by including a mixed-mode Paris law. In the absence of pure mode I and mode II experimental data, it was decided to modify the Paris law curve of the CLS specimen for mode I and mode II by changing the Paris law parameter  $C_1$ . Based on Equation (14),  $C_{1I}$  and  $C_{1II}$  were computed in a way that for the mixed mode ratio of the CLS specimen,  $C_{1CLS}$  is always given. Different fractions of  $C_{1II}/C_{1I}$  were then investigated and the results are summarized in Figure 7, where MMR-10 corresponds to  $C_{1II}/C_{1I} = 10$ . It was found that by accounting for mixed mode ratio in the Paris law, it is possible to improve the prediction of the experimental crack growth behavior.

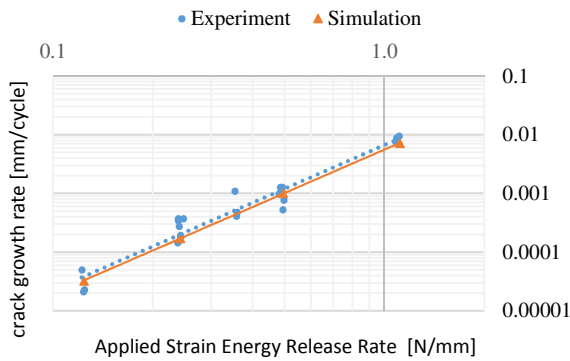


Figure 6: Paris Law

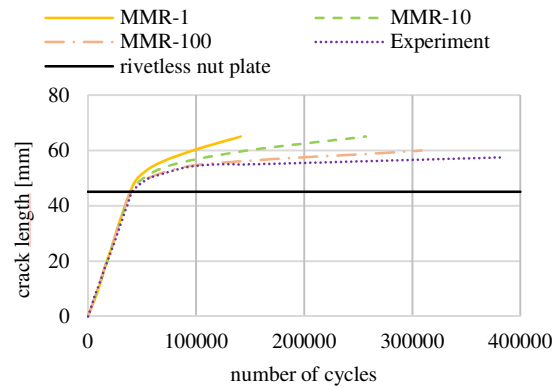


Figure 7: Crack growth behaviour of CLS-specimen including a rivetless nut plate joint

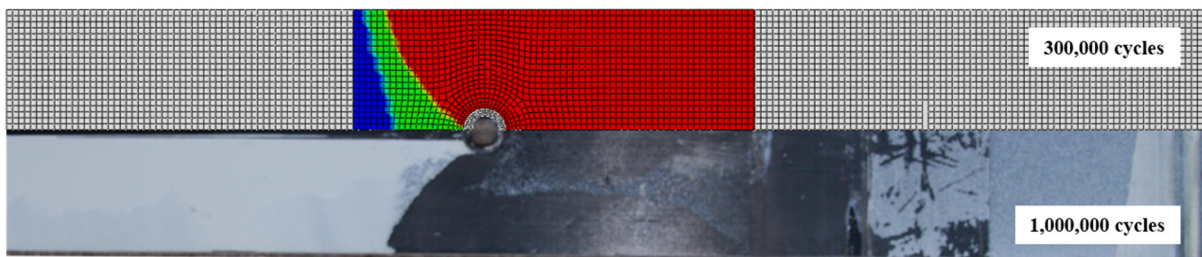


Figure 8: Comparison of crack front shape between numerical simulation and experimental test (failed elements colored red)

Furthermore, Figure 8 shows that the fatigue model is able to closely predict the shape of the curved crack front found in experiments. While the crack front shape is well captured, it must be noted that the number of fatigue cycles at which the crack front is compared in Figure 8 is not identical. This mismatch is assumed to be attributed to the absence of correct experimental results for the pure mode II Paris law curve.

## 5 CONCLUSIONS

A constitutive model to simulate the crack growth in adhesively bonded CFRP specimen subjected to fatigue loading has been developed. The model extends the static damage variable of a cohesive zone element by a scalar fatigue damage variable and determines a fatigue damage change based on the Paris law curve. By applying fatigue damage only to integration points of the crack tip, combined with several non-local algorithms, it has been possible to simulate crack growth of arbitrary shapes and under complex fatigue loading. The fatigue model has been applied to purely adhesively bonded CLS specimen at different load levels and was able to closely predict the experimental Paris law curve. Furthermore, the crack growth in an adhesively bonded CLS specimen with an additionally installed rivetless nut plate joint was modelled. It was found that including the mixed mode ratio effect in the Paris law curve allowed the simulation model to predict well complex crack growth compared to test measurements.

## 6 ACKNOWLEDGEMENT

The support of the European Union Seventh Framework Programme (FP7/2007-2013), under grant agreement n° 314180 (Project BOPACS: Boltless Assembling of Primary Aerospace Composite Structures), is gratefully acknowledged.

## References

- [1] Federal Aviation Administration, "AC 20-107B - Composite Aircraft Structures," 24 August 2010.
- [2] Boltless assembling Of Primary Composite Structures (BOPACS), "Description of Work," EU FP7 Research Project, 2012.
- [3] M. M. Abdel Wahab, "Fatigue in Adhesively Bonded Joints: A Review," *ISRN Materials Science*, vol. 2012, 2012.
- [4] I. A. Ashcroft, J. P. Casa-Rodriguez and V. V. Silberschmidt, "A Model to Predict the Anomalous Fatigue Crack Growth Behaviour Seen in Mixed Mechanism Fracture," *The Journal of Adhesion*, no. 86, pp. 522-538, 2010.
- [5] M. Fernández, M. de Moura, L. da Silva and A. Marques, "Mixed-mode I + II fatigue/fracture characterization of composite bonded joints using the Single-Leg Bending test," *Composites: Part A*, no. 44, pp. 63-69, 2013.
- [6] S. Stelzer, R. Jones and A. Brunner, "Interlaminar fatigue crack growth in carbon fiber reinforced composites," in *19th International Conference on Composite Materials*, Montréal, 2013.
- [7] "Cherry Aerospace," 6 10 2014. [Online]. Available: <http://cherryaerospace.com/>.
- [8] R. Sachse, A. K. Pickett, W. Adebahr, M. Klein, M. Käß and P. Middendorf, "Experimental investigation of mechanical fasteners regarding their influence on crack growth in adhesively bonded CFRP-joints subjected to fatigue loading," in *20th International Conference on Composite Materials*, Copenhagen, 2015.
- [9] A. Turon, J. Costa, P. Camanho and C. Davila, "Simulation of delamination in composites under high-cycle fatigue," *Composites: Part A*, no. 38, pp. 2270-2282, 2007.
- [10] P. W. Harper and S. R. Hallett, "A fatigue degradation law for cohesive interface elements - Development and application to composite materials," *International Journal of Fatigue*, no. 32, pp. 1774-1785, 2010.
- [11] F. Moroni and A. Pirondi, "A procedure for the simulation of fatigue crack growth in adhesively bonded joints based on the cohesive zone model and different mixed-mode propagation criteria," *Engineering Fracture Mechanics*, no. 78, pp. 1808-1816, 2011.
- [12] L. F. Kawashita and S. R. Hallett, "A crack tip tracking algorithm for cohesive interface element analysis of fatigue delamination propagation in composite materials," *International Journal of Solids and Structures*, no. 49, pp. 2898-2913, 2012.